Polymer 76 (2015) 220–229

Contents lists available at ScienceDirect

Polymer

journal homepage: www.elsevier.com/locate/polymer

Conjugated polymer/fullerene nanostructures through cooperative non-covalent interactions for organic solar cells

Fei Li [a], Noel M. Dawson [b], Ying-Bing Jiang [c], Kevin J. Malloy [b], Yang Qin [a, *]

[a] Department of Chemistry & Chemical Biology, University of New Mexico, MSC03 2060, 1 UNM, Albuquerque, NM 87131, United States
[b] Center for High Technology Materials, University of New Mexico, MSC04 2710, 1 UNM, Albuquerque, NM 87106, United States
[c] TEM Laboratory, University of New Mexico, Albuquerque, NM 87131, United States

ARTICLE INFO

Article history:
Received 30 June 2015
Received in revised form
1 September 2015
Accepted 2 September 2015
Available online 9 September 2015

Keywords:
Conjugated block copolymer
Complementary hydrogen bonding
Self-assembly

ABSTRACT

We have previously reported the formation of polymer/fullerene core–shell composite nanofibers (NFs) through self-assembly of functionalized conjugated block copolymers and fullerene derivatives, by cooperation of orthogonal non-covalent interactions including block copolymer phase separation, fullerene aggregation, poly(3-hexylthiophene) (P3HT) crystallization and complementary hydrogen bonding. These NFs displayed improved solar cell performances and the core–shell type structures are generally insensitive to polymer/fullerene weight ratios. In order to better understand the self-assembly mechanisms of such complex systems, we have prepared a new block copolymer (**P3**) having a different block length ratio and studied its solution and thin film morphologies in the presence of fullerene derivatives at different weight ratios. Worm-like micelles are observed for **P3** in mixed-solvent solutions, distinctly different from the well-defined NFs observed previously. Upon fullerene additions, the solution morphologies gradually change into hierarchically complex nanostructures with varying fullerene contents. Thin film morphologies are studied by atomic force microscopy (AFM) and the blends are applied in organic solar cell (OSC) devices. Our present studies provide detailed information on the self-assembly behaviors of conjugated block copolymers and fullerenes under cooperative orthogonal non-covalent interactions.

1. Introduction

Active layer morphologies in bulk-heterojunction (BHJ) organic solar cells (OSCs) have been shown to play a decisive role in device performance [1–7]. In general, bi-continuous donor/acceptor phases having dimensions at the nanometer scale are critical in achieving efficient charge separation and collection. State-of-the-art OSCs based on conjugated polymers (CPs) and fullerene derivatives are typically optimized thermally through trial-and-error approaches that are highly system dependent and generally very difficult to control. Morphologies in these devices are intrinsically in a thermodynamically meta-stable state that can induce macrophase separation and result in decreased device performance and reduced cell lifetimes [8–11].

Among various strategies to achieve stable and controllable BHJs in OSC devices, self-assembly of donor-acceptor type block copolymers (BCPs) are especially attractive owing to the ability to precisely control phase separation processes and organic/organic interfaces on the molecular level [12–18]. Most existing donor-acceptor BCPs contain fullerene moieties selectively attached to one block through covalent linkages [19–25]. Fullerene loading percentages in these polymers are generally low and hard to control because of the limited solubility and strong aggregation tendency of fullerenes. Unwanted cross-linking side-reactions via multiple additions on a single fullerene cage can sometimes be problematic. A clever alternative approach is to attach fullerene acceptors non-covalently. Fullerene loading percentages can thus be easily adjusted and solubility of the resulting complexes can be enhanced due to the reversible nature of these non-covalent interactions. Several recent reports have described complexation between fullerene derivatives and poly(3-hexylthiophene) (P3HT) based diblock and random copolymers through single-point hydrogen bonding (HB) [26–28] and π–π [29,30] interactions. Enhanced morphology stability was observed using these complexes as OSC active layers or as phase compatibilizers. However, single-point HB and π–π interactions are relatively weak. Among

* Corresponding author.
E-mail address: yangqin@unm.edu (Y. Qin).

http://dx.doi.org/10.1016/j.polymer.2015.09.005
0032-3861/

well-studied systems, complementary hydrogen bonding represents one of the strongest and most directional non-covalent interactions and has been widely applied in supramolecular chemistry [31–34]. Self-assembly of conjugated small molecules and polymers into various nanostructures modulated by complementary hydrogen bonding interactions has been well-studied and documented [35–44]. On the other hand, crystalline materials, especially crystalline CPs, are highly desired for better exciton/charge transport. However, crystallization of CPs can potentially complicate the self-assembly behaviors of conjugated BCPs. Furthermore, fullerene derivatives are by far the best electron acceptors in OSC devices and, at the same time, have strong aggregation tendency that can alter the phase behaviors of conjugate BCP donors. Thus, in order to apply the above mentioned morphology control methods, we need to have a good understanding of the combinatorial effects from several orthogonal non-covalent interactions working simultaneously [45], *i.e.*, conjugated BCP self-assembly, fullerene aggregation, CP crystallization and complementary HB. Such systems are seemingly very complex and have rarely been studied before, and thus general knowledge on cooperative control of these interactions is of great importance.

We have recently prepared two such systems as shown in Scheme 1A and 1B [46–49] and found that block length ratios of the polymers and nature of the fullerenes played crucial roles in morphology control and device performance. We initially prepared diaminopyrimidine functionalized block polythiophene **P1** having a block length ratio (unfunctionalized vs. functionalized) of ca. 2.5/1 and functionality of ca. 17%. A thymine tethered fullerene pyrrolidine **F1** was also synthesized, which forms strong complementary HBs with **P1**. OSC devices made from **P1**/**F1** blends showed poor performance and we thought the poor performance could have resulted from the pyrrolidine fullerene in **F1**, which have historically shown worse performances than the commonly applied phenyl-C_{61}-butyric acid methyl ester (PCBM) [50–53]. We thus prepared **P2**, having a larger block length ratio, and **F2** derived directly from PCBM, between which there are also strong three-point complementary HB interactions. Indeed, blends of **P2** and **F2** showed performance comparable to conventional P3HT/PCBM BHJ cells. However, additional **F2** or PCBM had to be added in order to achieve the optimal performance, making the final **P2**/**F2** and **P2**/**F2**/PCBM weight ratio 10/8 and 10/4/4, respectively. This is likely caused by the relatively small functionality of **P2** at ca. 7%. The **P2**/

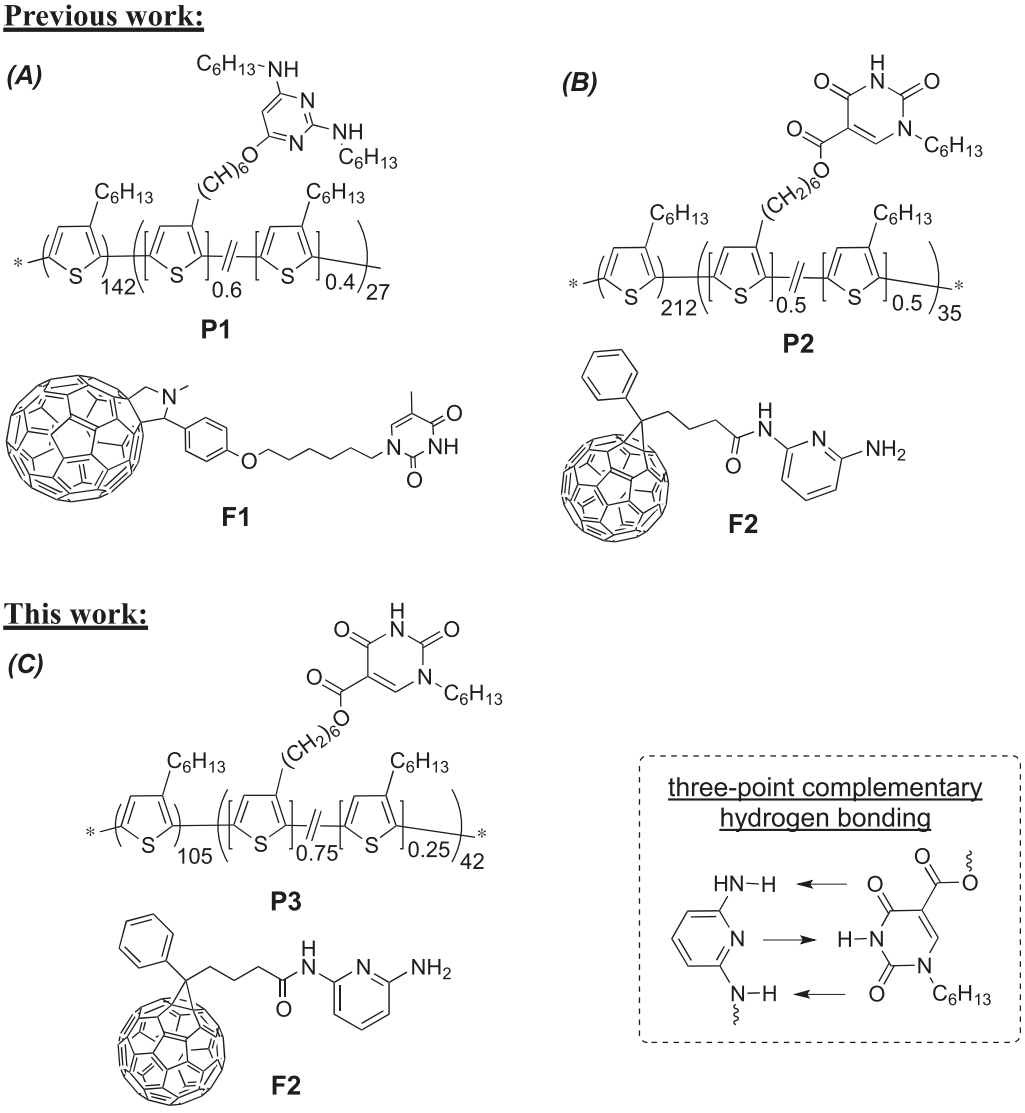

Scheme 1. Chemical structures of conjugated block copolymers and fullerene derivatives.

F2 weight ratio at 100% complexation is *ca.* 10/4, at which there may not be enough fullerene molecules in the blends to extract and conduct electrons efficiently. Intriguingly, **P2** core/fullerene shell type composite nanofibers (NFs) could be obtained in mixed solvents, which led to morphology controllability at both the microscopic and macroscopic level [48,49]. Such core–shell structures are generally insensitive to the polymer/fullerene weight ratios since only thicker NFs are obtained when larger amount of fullerenes are present.

In order to study in more detail the interplay among the block length ratios, functionality and fullerene loadings, we report herein a new block polythiophene **P3** (Scheme 1C), having similar block length ratio and functionality as those of **P1** but functionalized with isoorotic acid (IOA) moieties as those in **P2**, which can form three-point complementary HB interactions with **F2**. Besides the thin films from simple **P3**/**F2** blends, nanostructures formed from **P3**/**F2** solutions are also studied in detail. Corresponding OSC devices are fabricated and evaluated. We find that complex nanostructures can be obtained through cooperation of the orthogonal non-covalent interactions and the polymer/fullerene ratio is key in determining the appearances of nanostructures as well as the device performances.

2. Results and discussion

2.1. Synthesis and characterization

Synthesis of the 1-N-hexylisoorotic acid (IOA) functionalized block copolymer (**P3**) is shown in Scheme 2, similar to the methodology reported in our previous work. The synthetic details are presented in the Experimental Section and the ^{1}H NMR spectra and size exclusion chromatography (SEC) profiles of the polymers are included in Figure S1 of the Supporting Information (SI). During the synthesis, the **M1**/**M2** monomer feed ratio was set at 3/1, and **M2** was added when the conversion of **M1** reached ca. 90% in order to have a second block with higher **M2** content while still maintaining a statistical nature. As shown in Figure S1, integration of the methylene group signals at 3.61 ppm (–OCH_2–) and 2.80 ppm (Th–CH_2–) in the ^{1}H NMR spectrum of **P3** reveals the overall functionalization percentage to be ca. 22%, corresponding to ca. 88% conversion of **M2** during the chain-extension step. Molecular weights of **P3HT-Ni** (M_n = 17.4 kDa, *PDI* = 1.10) and **P-Si** (M_n = 28.7 kDa, *PDI* = 1.20) obtained from SEC analysis give a block length ratio of ca. 2.5 to 1, which is close to that reported previously for **P1**.

2.2. Optical, electrochemical and thermal properties

In order to investigate the influence of post-polymerization modification and polar functional groups on the electronic properties of P3HT, UV–vis absorption measurements were carried out on **P3** solutions and thin films (as-cast and thermally annealed) as shown in Figure S2. The solution absorption profile of **P3** displays a structureless peak with λ_{max} = 458 nm. For as-cast thin films of **P3**, a red shifted absorption peak at λ_{max} = 516 nm, accompanied by the appearance of vibronic shoulders at ca. 550 nm and ca. 600 nm, is observed. Such phenomenon is regularly observed in CPs due to aggregation in the solid state. Thermal annealing slightly enhances the organization of polymer chains as indicated by increased intensities of the vibronic shoulders. It is noted that the intensities of the vibronic shoulders observed in **P3** films are smaller than those observed in pure P3HT films, indicating the lower degree of crystallinity of the **P3** polymer backbone. This decreased crystallinity is likely due to inter- and intra-molecular hydrogen bonding interactions among the IOA moieties, which hinder efficient polymer packing. From the absorption edge of the spectrum of as-cast films, a bandgap of ca. 1.9 eV is estimated for **P3**, in good agreement with the optical bandgaps of **P1** and **P2**, as well as with reported values for P3HT [54,55]. Cyclic voltammetry (CV) measurements on **P3** films revealed a quasi-reversible oxidation with onset at +0.1 V (vs. Fc/Fc^+ redox couple) as shown in Figure S3, giving a HOMO level of ca. 4.9 eV below vacuum, identical with our measured values for **P1** and **P2** [46,47]. These observations imply that the higher percentage of IOA functionalities in **P3** does not noticeably change the electronic properties of the conjugated main-chains, compared with its lower percentage analog **P2** as well as **P1** functionalized

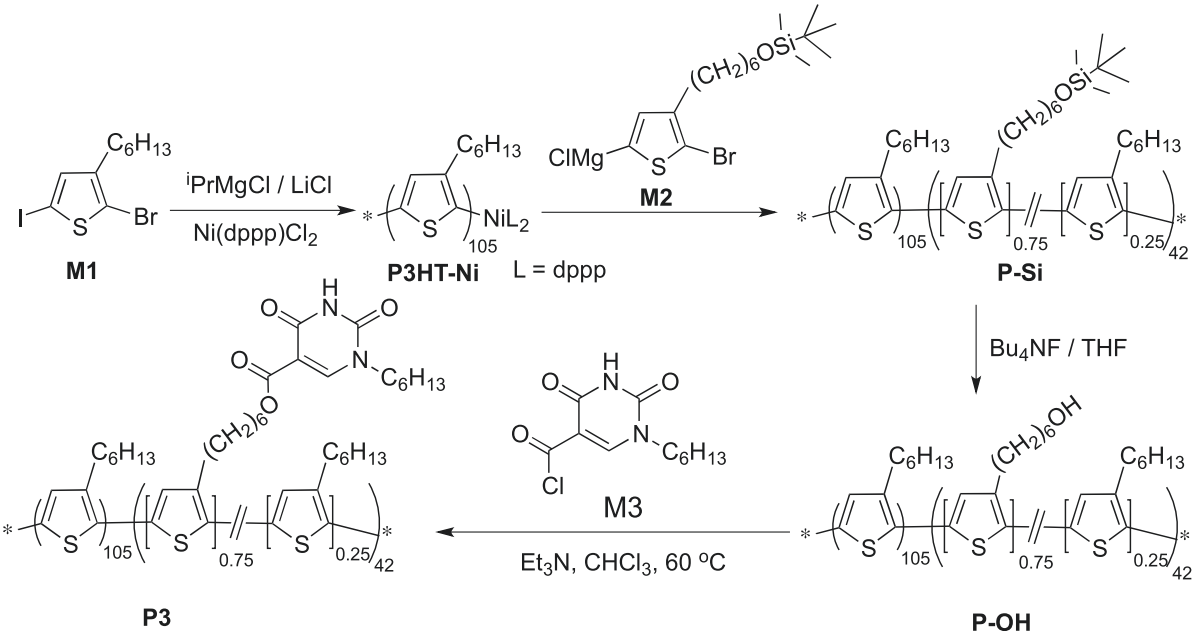

Scheme 2. Synthesis of **P3**.

with diaminopyrimidine moieties.

In order to probe the effects of higher density of the functional groups and the hydrogen bonding interactions among them on thermal properties of the polymer in the solid state, differential scanning calorimetry (DSC) measurements were performed on **P3** and its blend with **F2**, respectively. All samples (ca. 10 mg) were subjected to identical heating and cooling sequences (−50 °C–300 °C, 10 °C/min). The blend was obtained by dissolving **P3** and **F2** at a 1:1 M ratio (IOA:**F2**) in chloroform followed by extensive drying under vacuum. The second heating and first cooling curves were used for analysis as shown in Figure S4. **P3** shows a melting point at ca. 213 °C, about 9 °C lower than that of **P2** (ca. 222 °C). Upon mixing with **F2**, the melting point of the blend decreased to ca. 189 °C. These observations suggest a slightly less crystalline nature of **P3** than that of **P2**, probably due to a relatively shorter highly crystalline unfunctionalized P3HT block, which agrees well with the film UV–vis absorption analysis. When complexed with **F2**, the relative concentration of the P3HT block is further reduced and thus an even lower melting point is observed. On the other hand, the absorption and DSC results also suggest the amorphous nature of the functionalized block in **P3** with and without **F2** complexation, which is an important factor in controlling solution and film morphologies as discussed below.

2.3. Thin film studies

To investigate the morphology tunability, we first studied thin films of the **P3**/**F2** blends at different weight ratios by UV–vis spectroscopy and the absorption spectra are shown in Fig. 1.

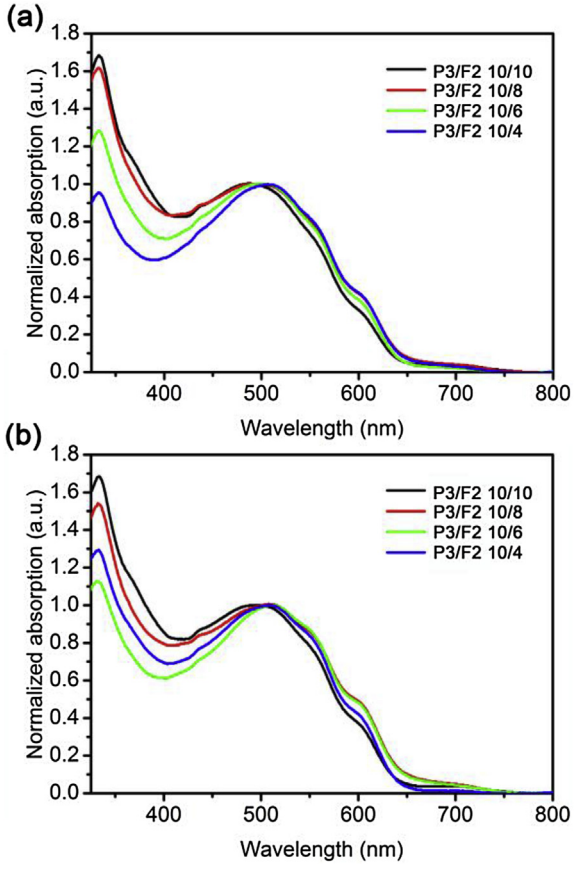

Fig. 1. UV–vis spectra of **P3**/**F2** blend films at different weight ratios: (a) as-cast; (b) annealed at 110 °C for 15 min.

The intensities of fullerene absorption at ca. 334 nm expectedly decrease with reduced **F2** content in the **P3**/**F2** as-cast films as shown in Fig. 1a. Also accompanying reduced **F2** contents, λ_{max}'s of the main P3HT absorption peaks gradually red-shift and the vibronic features become slightly enhanced. This trend is likely due to more fullerene molecules attached to the polymer through complementary HBs, making the unfunctionalized P3HT block less crystalline as discussed in the previous section. Upon thermal annealing, all blends show enhanced crystallinity evidenced by the more pronounced vibronic absorption features. Interestingly, the 10/8 and 10/6 films display similarly more enhanced vibronic structures than those of the 10/10 and 10/4 films (Fig. 1b), indicating more crystalline P3HT block in the former blends. We suspect that thermal annealing induces reorganization of the **P3**/**F2** complexes into thermodynamically more stable morphologies, the structures of which are highly dependent on the polymer fullerene weight ratios. As such, the 10/8 and 10/6 blends presumably exist in morphologies that have higher crystalline P3HT domains, while in the 10/10 and 10/4 blends, the P3HT block of **P3** is harder to crystallize.

In order to probe in more detail the nanostructural characteristics of these blend films, we performed X-ray diffraction (XRD) measurements. The scattering patterns are shown in Figure S5 and corresponding *d*-spacing's are presented in Table S1. All diffraction patterns display only one relatively sharp peak, corresponding to the polymer lamellar (100) packing. The lack of higher order scattering peaks indicates the less crystalline nature of **P3** than normal P3HT homopolymers as discussed earlier. Several trends are clearly observable. The scattering peaks are all sharper for thermally annealed films, which indicates enhanced crystallinity and is consistent with UV–vis measurements. While thermal annealing has negligible effects on the *d*-spacing's for pure **P3** films, *d*-spacing's for the blend films all increase after annealing, reflecting the effect of fullerene intercalation. Noticeably, *d*-spacing's for the 10/10 blends are larger than the other blends, indicating less efficient packing of the P3HT chains, which is consistent with the least pronounced vibronic features observed in the absorption measurements.

In order to visualize the morphological differences of these **P3**/**F2** blend films at different weight ratios, atomic force microscopy (AFM) was employed and the micrographs are shown in Fig. 2 and Figures S6–S8.

As seen in Figures S6 and S7, little difference can be observed in the **P3** films before and after thermal annealing, which is in line with the XRD measurements. The lack of fibril structures commonly observed in P3HT films confirms the less crystalline nature of **P3** due to HB interactions among IOA moieties. Clear differences are observed in the blend films as cast (Figure S8) and thermally annealed (Fig. 2). Upon thermal annealing, hydrogen bonding interactions and self-assembly between **P3** and **F2** played in cooperation to achieve more thermodynamically stable morphologies. The blend exhibits uniformly distributed short nanofiber morphology at a **P3**/**F2** weight ratio of 10/10, where all the active hydrogen bonding sites on **P3** are fully occupied by **F2** via the "three-point" hydrogen bonding interactions. The average domain size of such nanofibers is ca. 20 nm. Slight reduction of **P3**/**F2** weight ratio to 10/8 gives a coarser film and such nanofiber morphologies become less pronounced. We speculated that less **F2** attachment on **P3** could reduce the volume fraction of the block functionalized with hydrogen bonding moieties and fullerenes, and result in different self-assembly patterns. Meanwhile with less **F2** attachment, there are free IOA moieties remaining on the polymers, which can cross-link non-covalently and add another factor in morphology formation. Expectedly, further decreasing the **P3**/**F2** ratio to 10/6 and 10/4 leads to even less nanofiber features in the

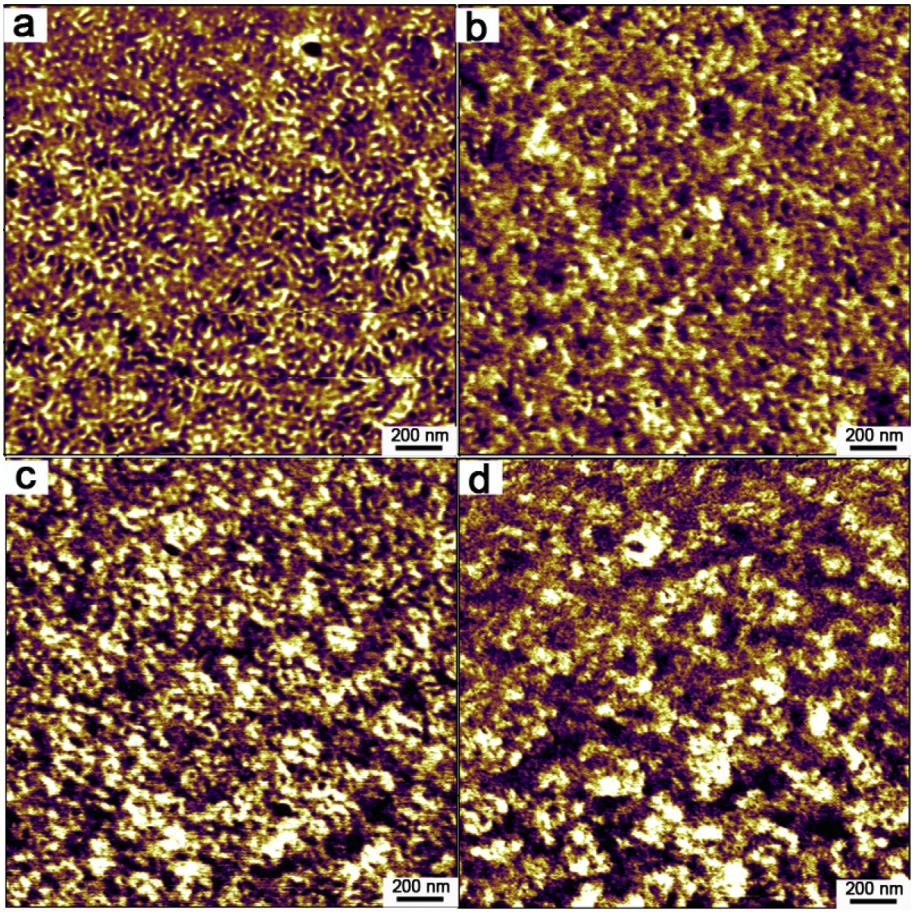

Fig. 2. AFM phase images (2 μm × 2 μm) of devices employing **P3** and **F2** at (a) 10/10; (b) 10/8; (c) 10/6; (d) 10/4 weight ratios, thermally annealed at 110 °C for 15 min.

film and the morphology of the 10/4 blend resembles that of **P3** itself as shown in Figure S6. These observations are very different from those observed in our previous studies with **P1** and **F1** under similar conditions, although the molecular weights and block length ratios of **P1** and **P3** are quite similar, indicating that the fullerene structures and the nature of HB do play significant roles in the self-assembly processes.

2.4. *Nanostructures of **P3/F2** mixtures in solutions*

Regio-regular poly(3-alkylthiophene)s (P3ATs) have been reported to form NFs in mixed-solvents by adding a "bad" solvent to a polymer solution in a "good" solvent. These NFs have shown improved solar cell performance due to the enhanced charge separation and transport efficiencies [25,56–58]. Yang and coworkers reported that P3HT could form NFs by slow addition of hexanes, a "bad" solvent, into well-dissolved P3HT solution in *o*-dichlorobenzene [59]. Cho and coworkers discovered another way of preparing P3HT NFs in the presence of PCBM by adding cyclohexanone into their chlorobenzene (CB) solutions [60]. The formation of P3HT NFs was indicated by the significantly enhanced vibronic peaks (ca. 560 nm and 600 nm) in their UV–vis absorption spectra. Thus, we have studied the nanostructure formation of **P3** in CB by adding hexanes, in which the HB interactions can potentially influence the self-assembly behavior.

With gradual addition of hexanes, λ_{max} of the UV–vis spectra of **P3** solution does not show significant differences until the hexanes/CB volume ratio reaches 1/2 (Figure S9), where a red-shift from 455 nm to 462 nm is observed as shown in Fig. 3a. Further increase of the hexanes volume fractions led to visual precipitation and thus we used the hexanes/CB volume ratio of 1/2 throughout the current study. Under such conditions, the red-shift in λ_{max} is relatively small and no appearance of vibronic structures can be observed, indicating P3HT backbones are not in a well-ordered state. We thus applied transmission electron microscopy (TEM) to explore the possibility of nanostructure formation and the TEM image is shown Fig. 3b. Worm-like fibers having lengths ranging from tens of nm to several hundred nm are observed. The average width of these NFs is 7.27 ± 0.73 nm, sampled from 200 individual objects. The appearance of these NFs is distinctly different from that of NFs formed from P3HT homopolymers that are rigid rod shaped and have average widths of 15–20 nm and lengths up to several microns [61,62]. We suspect that in our case, hexanes are a worse solvent for the IOA functionalized block in **P3** than for the P3HT block, with the functionalized block being the minority. Upon addition of hexanes, the functionalized block starts to aggregate, facilitated by inter- and intra-molecular HB interactions, forming the core of NFs. The P3HT block still remains solubilized and forms the shell component, which is still in a non-aggregated state.

We next studied nanostructure formation from **P3**/**F2** mixed at different weight ratios in the same mixed solvents. The UV–vis absorption spectra are shown in Fig. 4 and the TEM images in Fig. 5. While the polymer backbone is not significantly aggregated in the **P3** alone solutions, all the **P3**/**F2** solutions displayed vibronic patterns at ca. 560 nm and 610 nm as shown in Fig. 4a, indicating more enhanced aggregation through fullerene attachment. Such vibronic

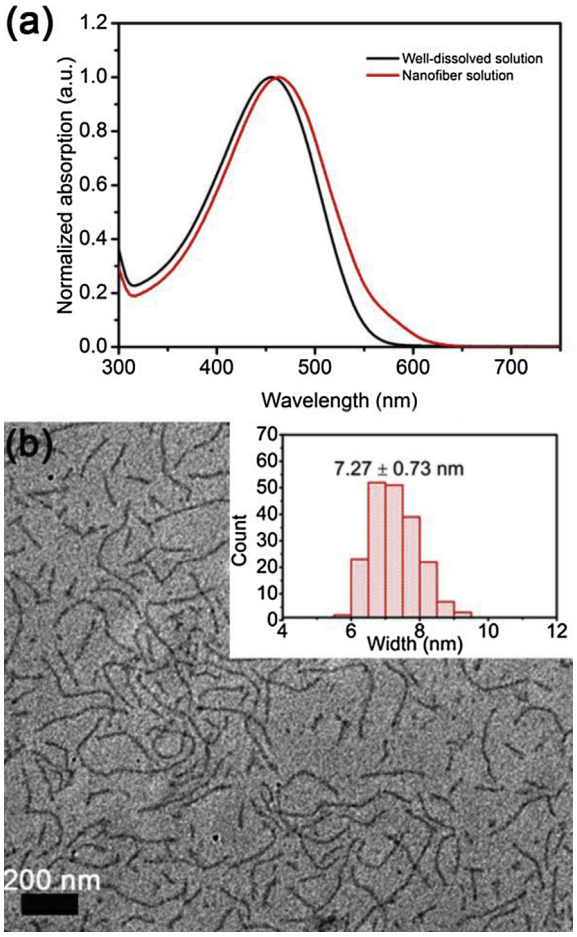

Fig. 3. (a) UV–vis spectra of **P3** in chlorobenzene (CB, 10 mg/mL, black) and after the addition of hexanes (1/2 hexanes/CB, vol./vol.); solutions were diluted 50 times with identical solvents before measurements; (b) transmission electron microscopy (TEM) image of **P3** grown from hexanes/CB (1/2, vol./vol.) solution (10 mg/mL). Insert: histogram of nanofibril widths sampled from 200 individual objects.

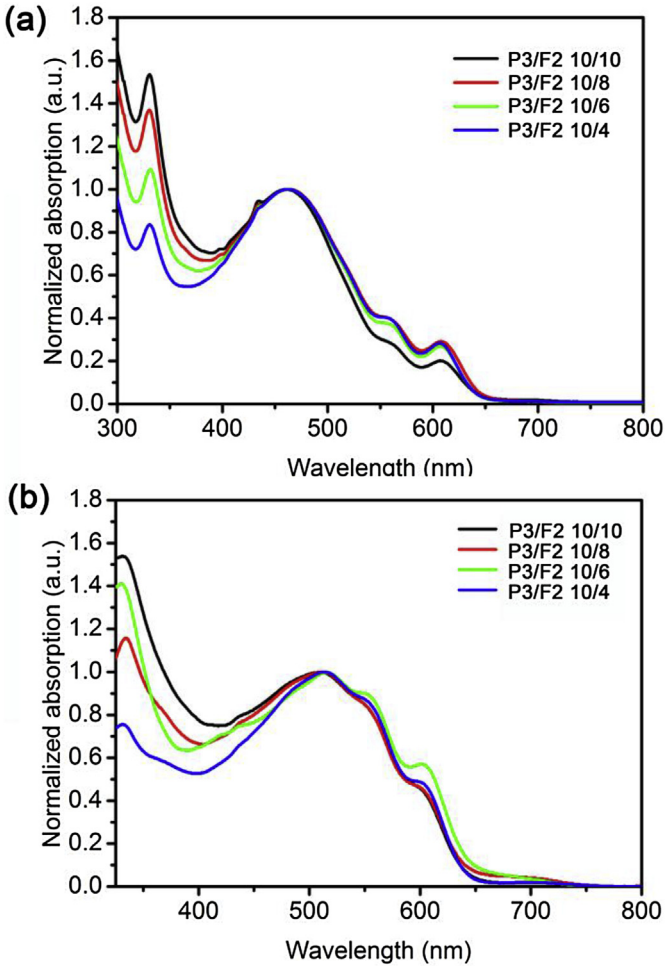

Fig. 4. UV–vis spectra of (a) solutions of **P3**/**F2** at different weight ratios in hexanes/CB (1/2 vol./vol.); and (b) thin films on glass substrates spin-cast from corresponding solutions, annealed at 150 °C for 15 min.

patterns are even more pronounced in their films as shown in Fig. 4b and Figure S10. It is likely that addition of **F2** occupies the IOA moieties on **P3**, which makes inter- and intra-molecular HB interaction from free IOA groups less effective and leads to more efficient packing of the unfunctionalized P3HT block.

To further study the mechanisms of self-assembly and identify the nanostructures formed from **P3** and **F2** complexation, we performed TEM measurements on the blend solutions and the results are summarized in Fig. 5. Distinctly different structures resulted from changing the polymer/fullerene ratios. In the 10/10 blend solutions (Fig. 5a), spherical and short fibril micelles having sizes of ca. 18 nm are observed, which is different from those narrower and longer fibers observed in **P3** solutions (Fig. 3b). Supposedly with this blend ratio, all the IOA groups on **P3** are occupied with **F2** through complementary HB, resulting in "bottle-brush" type BCP structures. Self-assembly of such BCP is thus controlled by the competition between P3HT crystallization and fullerene aggregation. We suspect that, due to the high functionality of **P3**, and thus a high volume fraction of the **F2** attached block, fullerene aggregation dominates the self-assembly processes leading to fullerene-cored P3HT-shelled spherical micelles. We have previously observed similar phenomena in the case of **P1**/**F1** complexes at a 10/10 weight ratio [46].

When the weight ratio of **P3**/**F2** is decreased to 10/8, uniform fibrils having average widths of ca. 14 nm are observed. By reducing the **F2** contents, the volume fraction of the functionalized block on **P3** is relatively reduced while fullerene aggregation and HB interactions among free IOA groups dominate the self-assembly process. As a result, cylindrical micelles are formed and we expect the core of the cylinders to be composed of the **F2** containing block surrounded by the unfunctionalized P3HT block. Upon further reducing the **P3**/**F2** weight ratio to 10/6, fibril/cylindrical micelle structures still predominate having, however, reduced average widths to ca. 11 nm, likely caused by the decrease in fullerene contents. Interestingly, large bundle-like structures are also observed in the solution, presumably due to the inter-micellar HB interactions between the more abundant IOA groups, which pull individual micelles together to form such secondary structures. Such effects are even more pronounced in the **P3**/**F2** (10/4) solutions as seen in Fig. 5d. High quality TEM images could not be obtained in this case, possibly caused by the more prevalent inter-micellar hydrogen bonding interactions that blur the boundaries among individual structures.

2.5. Solar cell fabrication and testing

In order to evaluate the effects of these orthogonal non-covalent interactions and nanostructure formation in modulating OSC performance, solar cell devices were fabricated, having active layers from both **P3**/**F2** chlorobenzene solutions (BHJ) and **P3**/**F2** hexanes/

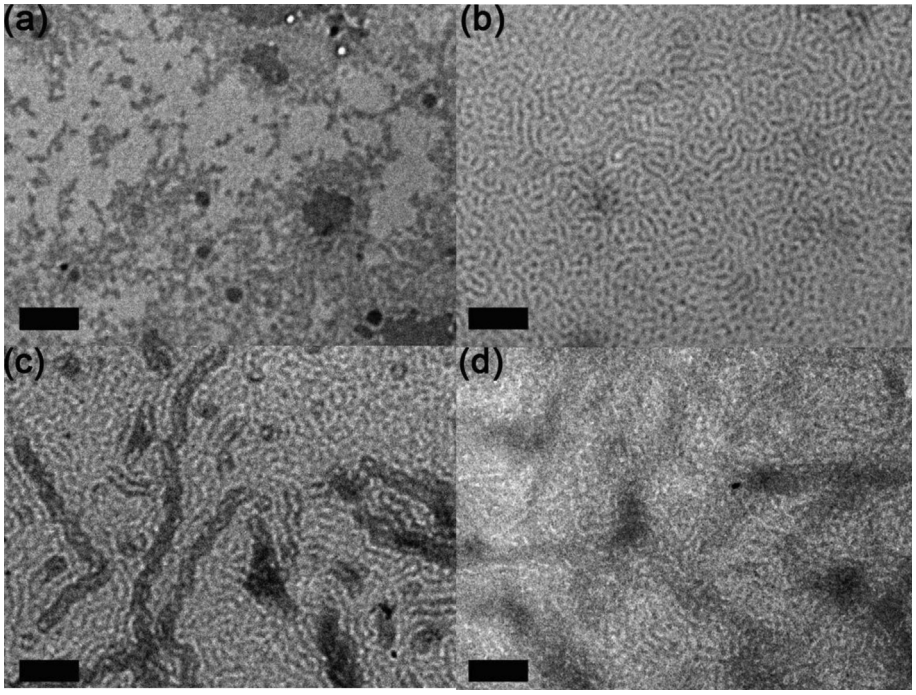

Fig. 5. TEM images of **P3/F2** solutions at different weight ratios in hexanes/CB (1/2 vol/vol): (a) 10/10; (b) 10/8; (c) 10/6; (d) 10/4. The concentration for **P3** is 10 mg/mL. The scale bar is 200 nm.

chlorobenzene (1/2 vol./vol., nanostructure) solutions. All solar cells adopted the structure of ITO/MoO_3 (10 nm)/active layer (ca. 100 nm)/Al (100 nm), which were constructed under identical conditions. Results from the BHJ devices are shown in Table 1 and Figure S11 and those for the nanostructured devices are shown in Table 2 and Figure S12.

For the BHJ devices, the 10/10 blends have the best photovoltaic performance with power conversion efficiencies (*PCE*s) of ca. 0.99% in as-cast devices and ca. 1.2% in thermally annealed devices, as shown in Table 1. Reducing the fullerene contents gradually decreases device efficiencies, reflected mostly from reduction in device short circuit current (J_{SC}). This is consistent with previous observations in which the optimal blend ratios of P3HT/PCBM in BHJ devices are ca. 1/1.

On the other hand, devices fabricated from **P3**/**F2** nanostructures show different trends. The 10/10 devices display the worst performance with the smallest J_{SC}'s and fill factors (*FF*s). This is easily understandable since spherical micelles are formed with this blending ratio (Fig. 5a) and the fullerene molecules are completely surrounded by P3HT chains, which leads to disconnected electron conduction pathways and thus severe charge recombination. The best performance is observed in the 10/8 devices that also out-perform the best BHJ devices in the current study. This is presumably due to the well-defined fibril/cylindrical micellar structures preformed in solutions. When cast into solid films, interconnections among these fibers can provide more continuous pathways for both hole and electron conduction, thus leading to higher photocurrents. Further reducing **F2** contents seems to decrease device performance, which can be explained by the less efficient electron conduction.

Table 1
Device performance data of BHJ **P3**/**F2** at different weight ratios.[a]

Condition	**P3/F2**[b]	*PCE* (%)[c]	J_{SC} (mA/cm^{-2})[c]	V_{OC} (V)[c]	*FF*[c]
As-cast	10:10	0.99 ± 0.05	4.68 ± 0.24	0.63 ± 0.00	0.33 ± 0.01
	10:8	0.81 ± 0.04	3.80 ± 0.20	0.64 ± 0.01	0.33 ± 0.01
	10:6	0.86 ± 0.10	3.90 ± 0.27	0.68 ± 0.02	0.32 ± 0.02
	10:4	0.46 ± 0.03	2.23 ± 0.09	0.68 ± 0.00	0.30 ± 0.01
Annealed[d]	10:10	1.20 ± 0.10	5.37 ± 0.32	0.65 ± 0.00	0.34 ± 0.01
	10:8	0.93 ± 0.06	4.14 ± 0.23	0.65 ± 0.01	0.35 ± 0.01
	10:6	0.91 ± 0.14	4.52 ± 0.39	0.65 ± 0.01	0.31 ± 0.02
	10:4	0.48 ± 0.02	2.75 ± 0.15	0.64 ± 0.01	0.28 ± 0.00

[a] Spin-cast at 400 rpm for 30 s from chlorobenzene solution, with 2 vol% MeOH added.
[b] All ratios by weight.
[c] An average of five cells.
[d] Thermal annealed at 110 °C for 15 min.

Table 2
Device performance data of **P3**/**F2** nanostructures at different weight ratios.[a]

Condition	**P3/F2**[b]	*PCE* (%)[c]	J_{SC} (mA/cm^{-2})[c]	V_{OC} (V)[c]	*FF*[c]
As-cast	10:10	0.56 ± 0.06	2.78 ± 0.09	0.67 ± 0.00	0.29 ± 0.02
	10:8	1.20 ± 0.05	5.04 ± 0.18	0.67 ± 0.01	0.36 ± 0.02
	10:6	0.90 ± 0.07	3.65 ± 0.34	0.68 ± 0.01	0.36 ± 0.01
	10:4	0.54 ± 0.04	2.83 ± 0.16	0.67 ± 0.01	0.29 ± 0.01
Annealed[d]	10:10	0.27 ± 0.00	2.13 ± 0.05	0.59 ± 0.01	0.21 ± 0.00
	10:8	1.67 ± 0.13	6.28 ± 0.38	0.66 ± 0.01	0.40 ± 0.01
	10:6	1.30 ± 0.07	5.97 ± 0.34	0.68 ± 0.00	0.32 ± 0.01
	10:4	0.54 ± 0.04	2.83 ± 0.16	0.67 ± 0.01	0.29 ± 0.01

[a] Spin-cast at 400 rpm for 30 s from hexanes/chlorobenzene (1/1, vol./vol.) solutions.
[b] All ratios by weight.
[c] Averages of five cells with standard deviations.
[d] Thermally annealed at 150 °C for 15 min.

3. Conclusion

In summary, we have successfully synthesized a polythiophene block copolymer **P3** functionalized with 22% IOA moieties. The higher functional group concentration on the polymer has minimum impact on the optical, electronic and thermal properties of the conjugated polymer. Tunable nanostructures can be obtained in solutions by simply varying the **P3**/**F2** weight ratios and such changes in morphologies are a result of cooperation of several non-covalent interactions including P3HT crystallization, fullerene aggregation and complementary hydrogen bonding. Preforming polymer/fullerene nanostructures has been shown to strongly influence solar cell performances and thus provides a viable way to further improve efficiencies of polymer based solar cells in general. We are currently optimizing the **P3**/**F2** nanostructures for solar cells by varying the non-covalent interaction conditions including block length ratios, functional group concentrations and selection of mixed solvents.

4. Experimental Section

4.1. Materials and general methods

All reagents and solvents were used as received from Sigma–Aldrich or Alfa Aesar unless otherwise noted. THF was distilled from Na/benzophenone prior to use. Anhydrous chloroform and dichloromethane were obtained by distillation over CaH_2 and degassed through several freeze–pump–thaw cycles. Monomers M1 and M2 were prepared according to previous procedures [46]. 300.13 MHz ^{1}H and 75.48 MHz ^{13}C NMR spectra were recorded on a Bruker Avance III Solution 300 spectrometer. All solution ^{1}H and ^{13}C NMR spectra were referenced internally to solvent signals. Size exclusion chromatography (SEC) analyses were performed in chloroform with 0.5% (v/v) triethylamine (1 mL/min) using a Waters Breeze system equipped with a 2707 autosampler, a 1515 isocratic HPLC pump and a 2414 refractive index detector. Two styragel columns (Polymer Laboratories; 5 μm Mix-C), which were kept in a column heater at 35 °C, were used for separation. The columns were calibrated with polystyrene standards (Varian). Ultraviolet–Visible (UV–Vis) absorption spectra were recorded on a Shimadzu UV-2401 PC spectrometer over a wavelength range of 240–800 nm. Fluorescence emission spectra were obtained using a Varian Cary Eclipse Fluorimeter. Differential scanning calorimetry (DSC) measurements were performed on a Mettler Toledo DSC STAR^e system with ca. 10 mg sample and at a scan rate of 10 °C/min. The results reported are from the second heating cycle. High resolution mass spectrometry (HRMS) was performed on a Waters/Micromass LCT Premier system operating under electrospray ionization (ESI) mode. Cyclic Voltammetry was performed at 25 °C on a CH Instrument CHI604xD electrochemical analyzer using a glassy carbon working electrode, a platinum wire counter electrode and a Ag/AgCl reference electrode calibrated using ferrocene redox couple (4.8 eV below vacuum). Atomic force microscopy (AFM) images were obtained on an Asylum MFP3D AFM instrument operated under tapping mode. Transmission electron microscopy (TEM) images were taken on a JEOL 2010 high resolution TEM operated under 200 kV. Thin film X-ray diffraction (XRD) patterns were recorded on a Rigaku SmartLab diffractometer.

4.2. P-Si

Two three-neck round-bottom flasks (250 mL and 50 mL) equipped with stopcocks and septa were flame-dried under high vacuum and cooled to room temperature under N_2. Monomer **M1** (1.48 g, 3.97 mmol) and LiCl (168 mg, 3.97 mmol) were placed in the 250 mL flask under N_2, and evacuated under high vacuum to remove any residual water and oxygen. After adding dry THF (40 mL) into the flask via a syringe, the solution was cooled to 0 °C. A 2 M solution of *i*-PrMgCl in THF (2 mL, 4 mmol) was added via syringe and the mixture was stirred at 0 °C for 30 min (solution 1). In the other 50 mL flask, 0.67 g (1.32 mmol) of 3-(6'-dimethyl-tert-butylsilyloxyl)hexylthiophene was first reacted with 0.67 mL of *i*-PrMgCl in the presence of 56 mg of LiCl (1.3 mmol) in 20 mL THF (solution 2) to yield **M2**. Solution 1 was heated up to 35 °C and Ni(dppp)Cl_2 catalyst (21 mg, 0.039 mmol), which was suspended in 5 mL dry THF, was added in one portion. The reaction mixture was stirred at 35 °C for 12 min, an aliquot was withdrawn with a syringe and injected into a methanol solution to give **P3HT-Ni** for SEC analysis (RI, $CHCl_3$, 1 mL/min: **P3HT-Ni** M_n = 17.4 kDa, M_w = 19.1 kDa, *PDI* = 1.1). Solution 2 containing **M2** was transferred to solution **1** via a cannula. The resulting red solution was stirred at 35 °C for 40 min before 0.5 mL of EtMgCl solution (2 M in THF) was added. The polymer was isolated by precipitation into MeOH and successively washed by Soxhlet extraction using methanol, acetone, and chloroform. The polymer was recovered by precipitation of the chloroform solution into methanol and dried under high vacuum to give a black solid (0.86 g, 89%). ^{1}H NMR (300.13 MHz, $CDCl_3$): δ (ppm) = 0.041 (s), 0.070 (s), 0.89–0.94 (m), 1.25–1.71 (m), 2.81(t, $^3J_{HH}$ = 7.5 Hz), 3.61 (t, $^3J_{HH}$ = 6.5 Hz), 6.98 (s). SEC (RI, $CHCl_3$ 1 mL/min): M_n = 28.7 kDa, M_w = 34.5 kDa, *PDI* = 1.2;

4.3. P-OH

To a 100 mL Schlenk flask was added 750 mg of polymer **P-Si** and 100 mL of THF under N_2. The solution became clear after stirring at 60 °C for ca. 30 min. Tetrabutylammonium fluoride (TBAF) solution (2 mL, 2 M in THF) was added dropwise via syringe. The reaction mixture was kept stirring at 60 °C for 8 h and concentrated under reduced pressure to ca. 5 mL. **P-OH** was recovered as a black solid by precipitation into a mixture of methanol and acetone (1/1, v/v) and dried under vacuum overnight (650 mg, 88%). ^{1}H NMR (300.13 MHz, $CDCl_3$): δ (ppm) = 0.92 (t, $^3J_{HH}$ = 7.5 Hz), 1.25–1.73 (m), 2.04 (s), 2.81 (t, $^3J_{HH}$ = 7.5 Hz), 3.66 (t, $^3J_{HH}$ = 6.5 Hz), 6.98 (s). SEC (RI, $CHCl_3$ 1 mL/min): M_n = 25.5 kDa, M_w = 30.2 kDa, *PDI* = 1.2.

4.4. P3

To a 25 mL three-neck flask equipped with a condenser and septa was added 246 mg (1.0 mmol) of 1-N-hexylisoorotic acid and 2 mL of thionyl chloride under nitrogen, and the solution was refluxed for 8 h to give the corresponding acid chloride. The excess $SOCl_2$ was removed in vacuo and the residue was dissolved in 10 mL of dry $CHCl_3$ and the solvent was removed under reduced pressure to get rid of the residual $SOCl_2$. In another 250 mL Schlenk flask was added 200 mg of **P-OH** and 30 mL of $CHCl_3$ under nitrogen. The reaction mixture was kept stirring at 60 °C for 20 min until all polymer dissolved and then triethylamine (0.3 mL) was added. The acid chloride was dissolved in 15 mL of $CHCl_3$ and transferred into the polymer solution via cannula. The reaction was kept at 60 °C for another 8 h and concentrated under reduced pressure to ca. 5 mL. The crude polymer was isolated by precipitation into methanol and successively Soxhlet extracted using methanol, acetone, and chloroform. The chloroform solution was concentrated and precipitated into MeOH to give **P3** (200 mg, 78%). ^{1}H NMR (300.13 MHz, $CDCl_3$): δ (ppm) = 0.89 (t, $^3J_{HH}$ = 7.5 Hz), 1.25–1.71 (m), 2.80 (t, $^3J_{HH}$ = 7.5 Hz), 3.77 (t, $^3J_{HH}$ = 7.5 Hz), 4.29 (t, $^3J_{HH}$ = 6.0 Hz), 6.98 (s), 8.20 (s). SEC (RI, $CHCl_3$ 1 mL/min): M_n = 30.6 kDa, M_w = 37.9 kDa, *PDI* = 1.3.

4.5. Nanostructure formation

In a dry vial was added 5 mg of **P3**, which was dissolved in 0.5 mL of chlorobenzene. The solution was heated at 100 °C for 1 h in a nitrogen glovebox and then stirred at room temperature for another 1 h. Hexanes (250 μL) were added dropwise via a microsyringe. The solution continued to age with stirring at room temperature for another 24 h before analysis. The color change of the solution indicated the formation of the micelles. The **P3**/**F2** nanostructures at different weight ratios were prepared using the same methods with the **P3** concentration held constant at 10 mg/mL.

4.6. Solar cell fabrication and testing

Solar cell devices adopt a structure of ITO/MoO_3/active layer/Al. Thin films of active layers were spun-cast from blend solutions and all solutions were prepared in a nitrogen glovebox (Innovative Technology, model PL-He-2GB, O_2 < 0.1 ppm, H_2O < 0.1 ppm) before device fabrication. Solar cell devices were fabricated according to the following procedure: ITO-coated glass substrates (China Shenzhen Southern Glass Display. Ltd, 8 Ω/□) were cleaned by ultrasonication sequentially in detergent, DI water, acetone and isopropyl alcohol, each for 15 min. These ITO-coated glass substrates were treated by UV-ozone (PSD Series, Novascan) for 45 min before being transferred to a nitrogen glove box (Innovative Technology, model PL-He-4GB-1800, O_2 < 0.1 ppm, H_2O < 0.1 ppm) for MoO_3 deposition. MoO_3 (10 nm) was deposited using an Angstrom Engineering Åmod deposition system at a base vacuum level < 7×10^{-8} Torr. Unfiltered **P3**/**F2** blend solutions were spin-coated on top of the MoO_3 layer at 400 rpm for 30 s. Al (100 nm) was thermally evaporated through patterned shadow masks as anodes. Current–voltage (I–V) characteristics were measured by a Keithley 2400 source-measuring unit under simulated AM 1.5G irradiation (100 mW/cm^{-2}) generated by a Xe arc-lamp based Newport 67005 150-W solar simulator equipped with an AM1.5G filter. The light intensity was calibrated by a Newport thermopile detector (model 818P-010-12) equipped with a Newport 1916-C Optical Power Meter.

Conflict of interest

The authors declare no competing financial interest.

Acknowledgment

The authors would like to acknowledge University of New Mexico and NSF (DMR-1453083) for financial support for this research.

Appendix A. Supplementary information

Supplementary information related to this article can be found at http://dx.doi.org/10.1016/j.polymer.2015.09.005.

References

[1] L.-M. Chen, Z. Hong, G. Li, Y. Yang, Adv. Mater. 21 (2009) 1434–1449.
[2] S. van Bavel, S. Veenstra, J. Loos, Macromol. Rapid Commun. 31 (2010) 1835–1845.
[3] C.J. Brabec, M. Heeney, I. McCulloch, J. Nelson, Chem. Soc. Rev. 40 (2011) 1185–1199.
[4] M. Wang, F. Wudl, J. Mater. Chem. 22 (2012) 24297–24314.
[5] K. Vandewal, S. Himmelberger, A. Salleo, Macromolecules 46 (2013) 6379–6387.
[6] M.T. Dang, L. Hirsch, G. Wantz, J.D. Wuest, Chem. Rev. 113 (2013) 3734–3765.
[7] F. Liu, Y. Gu, X. Shen, S. Ferdous, H.-W. Wang, T.P. Russell, Prog. Polym. Sci. 38 (2013) 1990–2052.
[8] M. Jørgensen, K. Norrman, F.C. Krebs, Sol. Energy Mater. Sol. Cells 92 (2008) 686–714.
[9] M. Jørgensen, K. Norrman, S.A. Gevorgyan, T. Tromholt, B. Andreasen, F.C. Krebs, Adv. Mater 24 (2012) 580–612.
[10] S. Bertho, G. Janssen, T.J. Cleij, B. Conings, W. Moons, A. Gadisa, J. D'Haen, E. Goovaerts, L. Lutsen, J. Manca, D. Vanderzande, Sol. Energy Mater. Sol. Cells 92 (2008) 753–760.
[11] B. Conings, S. Bertho, K. Vandewal, A. Sense, J. D'Haen, J. Manca, R.A.J. Janssen, Appl. Phys. Lett. 96 (2010) 163301.
[12] H. Jiang, Macromol. Rapid Commun. 31 (2010) 2007–2034.
[13] M. Sommer, S. Huettner, M. Thelakkat, Adv. Polym. Sci. 228 (2010) 123–153.
[14] M. Sommer, S. Huettner, M. Thelakkat, J. Mater. Chem. 20 (2010) 10788–10797.
[15] M. He, F. Qiu, Z. Lin, J. Mater. Chem. 21 (2011) 17039–17048.
[16] C.-L. Liu, C.-H. Lin, C.-C. Kuo, S.-T. Lin, W.-C. Chen, Prog. Polym. Sci. 36 (2011) 603–637.
[17] J. Roncali, Adv. Energy Mater 1 (2011) 147–160.
[18] P.D. Topham, A.J. Parnell, R.C. Hiorns, J. Polym. Sci. Pt. B Polym. Phys. 49 (2011) 1131–1156.
[19] S. Barrau, T. Heiser, F. Richard, C. Brochon, C. Ngov, K. van de Wetering, G. Hadziioannou, D.V. Anokhin, D.A. Ivanov, Macromolecules 41 (2008) 2701–2710.
[20] M. Sommer, A.S. Lang, M. Thelakkat, Angew. Chem. Int. Ed. 47 (2008) 7901–7904.
[21] J.U. Lee, A. Cirpan, T. Emrick, T.P. Russell, W.H. Jo, J. Mater. Chem. 19 (2009) 1483–1489.
[22] B. Gholamkhass, T. Peckham, S. Holdcroft, Polym. Chem. 1 (2010) 708–719.
[23] M. Dante, C. Yang, B. Walker, F. Wudl, T.-Q. Nguyen, Adv. Mater. 22 (2010) 1835–1839.
[24] S. Miyanishi, Y. Zhang, K. Tajima, K. Hashimoto, Chem. Commun. 46 (2010) 6723–6725.
[25] S.-H. Chan, C.-S. Lai, H.-L. Chen, C. Ting, C.-P. Chen, Macromolecules 44 (2011) 8886–8891.
[26] S.-L. Hsu, C.-M. Chen, Y.-H. Cheng, K.-H. Wei, J. Polym. Sci. A Polym. Chem. 49 (2011) 603–611.
[27] Y. Lin, J.A. Lim, Q. Wei, S.C.B. Mannsfeld, A.L. Briseno, J.J. Watkins, Chem. Mater 24 (2012) 622–632.
[28] K. Yao, L. Chen, F. Li, P. Wang, Y. Chen, J. Phys. Chem. C 116 (2012) 714–721.
[29] Y.-C. Lai, K. Ohshimizu, A. Takahashi, J.-C. Hsu, T. Higashihara, M. Ueda, W.-C. Chen, J. Polym. Sci. Pt. A Polym. Chem. 49 (2011) 2577–2587.
[30] L. Chen, S. Peng, Y. Chen, ACS Appl. Mater. Interfaces 6 (2014) 8115–8123.
[31] T.F.A. De Greef, M.M.J. Smulders, M. Wolffs, A.P.H.J. Schenning, R.P. Sijbesma, E.W. Meijer, Chem. Rev. 109 (2009) 5687–5754.
[32] M. Fathalla, C.M. Lawrence, N. Zhang, J.L. Sessler, J. Jayawickramarajah, Chem. Soc. Rev. 38 (2009) 1608–1620.
[33] S.K. Yang, A.V. Ambade, M. Weck, Chem. Soc. Rev. 40 (2011) 129–137.
[34] Y. Matsushita, A. Noro, A. Takano, Polym. J. 44 (2012) 72–82.
[35] P. Bäuerle, A. Emge, Adv. Mater 3 (1998) 324–330.
[36] A. Emge, P. Bäuerle, Synth. Met. 102 (1999) 1370–1373.
[37] E.E. Neuteboom, E.H.A. Beckers, S.C.J. Meskers, E.W. Meijier, R.A.J. Janssen, Org. Biomol. Chem. 1 (2003) 198–203.
[38] H. Fang, Z. Shi, Y. Li, S. Xiao, H. Li, H. Liu, D. Zhu, Synth. Met. 135–136 (2003) 843–844.
[39] H. Fang, S. Wang, S. Xiao, J. Yang, Y. Li, Z. Shi, H. Li, H. Liu, S. Xiao, D. Zhu, Chem. Mater 15 (2003) 1593–1597.
[40] C.-H. Huang, N.D. McClenaghan, A. Kuhn, G. Bravic, D.M. Bassani, Tetrahedron 62 (2006) 2050–2059.
[41] R. Hoogenboom, D. Fournier, U.S. Schubert, Chem. Commun. (2008) 155–162.
[42] M. Murakami, K. Ohkubo, T. Hasobe, V. Sgobba, D.M. Guldi, F. Wessendorf, A. Hirsch, S. Fukuzumi, J. Mater. Chem. 20 (2010) 1457–1466.
[43] D. González-Rodríguez, P.G.A. Janssen, R. Martín-Rapún, I. De Cat, S. De Feyter, A.P.H.J. Schenning, E.W. Meijer, J. Am. Chem. Soc. 132 (2010) 4710–4719.
[44] D. González-Rodríguez, A.P.H.J. Schenning, Chem. Mater 23 (2011) 310–325.
[45] M.L. Saha, S. De, S. Pramanik, M. Schmittel, Chem. Soc. Rev. 42 (2013) 6860–6909.
[46] F. Li, J. Yang, Y. Qin, J. Polym. Sci. A Polym. Chem. 51 (2013) 3339–3350.
[47] F. Li, K.G. Yager, N.M. Dawson, J. Yang, K.J. Malloy, Y. Qin, Macromolecules 46 (2013) 9021–9031.
[48] F. Li, K.G. Yager, N.M. Dawson, Y.-B. Jiang, K.J. Malloy, Y. Qin, Chem. Mater. 26 (2014) 3747–3756.
[49] F. Li, K.G. Yager, N.M. Dawson, Y.-B. Jiang, K.J. Malloy, Y. Qin, Polym. Chem. 6 (2015) 721–731.
[50] N. Camaioni, G. Ridolfi, G. Casalbore-Miceli, G. Possamai, M. Maggini, Adv. Mater. 14 (2002) 1735–1738.
[51] K. Matsumoto, K. Hashimoto, M. Kamo, Y. Uetani, S. Hayase, M. Kawatsura, T. Itoh, J. Mater. Chem. 20 (2010) 9226–9230.
[52] B.-Y. Ren, C.J. Ou, C. Zhang, Y.-Z. Chang, M.-D. Yi, J.-Q. Liu, L.-H. Xie, G.-W. Zhang, X.-Y. Deng, S.-B. Li, W. Wei, W. Huang, J. Phys. Chem. C 116 (2012) 8881–8887.
[53] N. Wang, X. Bao, C. Yang, J. Wang, H.Y. Woo, Z. Lan, W. Chen, R. Yang, Org. Electron 14 (2013) 682–692.
[54] P.-T. Wu, G. Ren, C. Li, R. Mezzenga, S.A. Jenekhe, Macromolecules 42 (2009) 2317–2320.
[55] J. Hou, T.L. Chen, S. Zhang, L. Huo, S. Sista, Y. Yang, Macromolecules 42 (2009) 9217–9219.

[56] S. Berson, R. De Bettignies, S. Bailly, S. Guillerez, Adv. Funct. Mater. 17 (2007) 1377–1384.
[57] M. Baghgar, J. Labastide, F. Bokel, I. Dujovne, A. McKenna, A.M. Barnes, E. Pentzer, T. Emrick, R. Hayward, M.D. Barnes, J. Phys. Chem. Lett. 3 (2012) 1674–1679.
[58] M. He, J. Ge, M. Fang, F. Qiu, Y. Yang, Polymer 51 (2010) 2236–2243.
[59] L. Li, G. Lu, X. Yang, J. Mater. Chem. 18 (2008) 1984–1990.
[60] J.-H. Kim, J.H. Park, J.H. Lee, J.S. Kim, M. Sim, C. Shim, K. Cho, J. Mater. Chem. 20 (2010) 7398–7405.
[61] K.J. Ihn, J. Moulton, P. Smith, J. Polym. Sci. Pt. B Polym. Phys. 31 (1993) 735–742.
[62] J. Liu, M. Arif, J. Zou, S.I. Khondaker, L. Zhai, Macromolecules 42 (2009) 9390–9393.